A magnetic bilateral tele-manipulation system using paramagnetic microparticles for micromanipulation of nonmagnetic objects

Seif, Mohamed Abou; Hassan, Amr; El-Shaer, Ahmed H.; Alfar, Abdelrahman; Misra, Sarthak; Khalil, Islam S.M.

Published in:
2017 IEEE International Conference on Advanced Intelligent Mechatronics, AIM 2017

DOI:
10.1109/AIM.2017.8014165

2017 IEEE International Conference on Advanced Intelligent Mechatronics (AIM)
Sheraton Arabella Park Hotel, Munich, Germany, July 3-7, 2017

A Magnetic Bilateral Tele-manipulation System using Paramagnetic Microparticles for Micromanipulation of Nonmagnetic Objects

Mohamed Abou Seif*, Amr Hassan*, Ahmed H. El-Shaer†,
Abdelrahman Alfar*, Sarthak Misra‡§, and Islam S. M. Khalil*

***Abstract*— This study presents a scaled-bilateral tele-manipulation system for magnetic-based control of paramagnetic microparticles. This bilateral control system consists of a haptic device (master-robot) and an electromagnetic system with four orthogonal electromagnetic coils. The electromagnetic system generates magnetic field gradients to control the motion of the microparticle (slave-microrobot). A systematic robust tele-manipulation control design of the microparticles is achieved using disturbance observers (DOBs) to estimate the interaction forces at both the master-robot and slave-microrobot. Experimental results show that point-to-point motion control of the slave-microrobots results in maximum position error of 8 μm in the steady-state. Furthermore, we demonstrate experimentally that interaction forces of tens of micro Newtons, between the slave-microrobot and non-magnetic microbeads, can be estimated using DOBs and scaled-up to the sensory range of the operator.**

I. Introduction

Magnetic micro- and nano-robotic systems are expected to have a wide spectrum of nano-technology [1]-[3] and nano-medicine [4]-[7] applications. Paramagnetic microparticles can be coated with drugs and localized under the influence of the magnetic field gradient within the vicinity of a deep-seated region of the human body. This microrobotic system allows for the elimination of direct human involvement in complex biological manipulations, and hence decreases the low reproducibility of manual results and possibility of contamination. Nevertheless, there exist many situations where it is essential to benefit from the precision of robotic systems while keeping a physician in control. Very recently, Lu *et al*. have presented a haptic interface that has a uniform response over the entire human tactile frequency range. This haptic interface enables the operator to feel interaction forces arising from contact with a microbead without visual feedback [8]. Pillarisetti *et al.* have developed an interface using a haptic device and a polyvinylidene fluoride film to measure contact forces of a few milli Newtons [9]. In addition, the positive effect of force feedback has been verified in cell injection [10]. Sun *et al.* have also developed an autonomous microrobotic injection system using a hybrid control approach with visual servoing and precision position control [11]. Kummer *et al.* have incorporated a hypodermic needle tip to an NdFeB agent, and used the OctoMag configuration to puncture vasculature on a CAM blood vessels in an *in vitro* chicken embryo [12]. Although this *in vitro* experiment is done by an operator based on visual feedback, the interaction forces between the magnetic agent and the blood vessels are not measured and fed back to the control system. This force measurement is essential in the realization of motion control systems for safe interaction with biological tissue and blood vessels. Bolopion *et al.* have used haptic feedback to achieve microassmebly of microbeads in three-dimensional space using Atomic Force Microscopy [13], and a dual-tip gripper is used for grasping and pick-and-place operations. However, the dependency on grasping is a significant functional limitation at microscale. Grasping

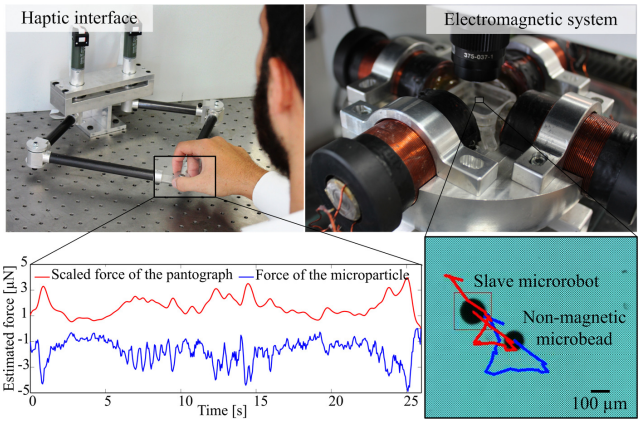

Fig. 1. A bilateral tele-manipulation system for the magnetic-based control of paramagnetic microparticles (slave-microrobots) and non-magnetic microbeads. The system consists of a pantograph haptic interface (master-robot) and an electromagnetic system with 4 electromagnetic coils. A scaled-bilateral control system is implemented between the master-robot and slave-microrobot to control the position of the non-magnetic microbead. Interaction forces between the slave-microrobot and the microbeads are estimated and scaled-up to the sensory range of the operator. The operational workspaces of the haptic device and the electromagnetic system are 10 cm $\times$10 cm and 1 mm $\times$ 1 mm, respectively.

This work was supported by the Science and Technology Development Fund in Egypt (No. 23016) and the DAAD-BMBF funding project.

*The authors are affiliated with the German University in Cairo, New Cairo City 11835, Egypt.

†Dana Holding Corporation, Maumee, Ohio 43537, USA.

‡Department of Biomechanical Engineering, MIRA–Institute for Biomedical Technology and Technical Medicine, University of Twente, Enschede 7500 AE, The Netherlands.

§Department of Biomedical Engineering, University of Groningen and University Medical Centre Groningen, Groningen 9700 RB, The Netherlands.

decreases the occurrence of successful releases in nanotechnology applications, and may result in contamination of samples in several biomedical applications. In this work, we expand on our previous proof-of-concept study [14], analyze the position and force tracking errors of a scaled-bilateral tele-manipulation system (Fig. 1), and achieve the following: (1) Scaled bilateral tele-manipulation [13] of paramagnetic microparticles using a haptic device based on disturbance observers (DOBs) to estimate the interaction forces with the master-robot and slave-microrobot [15], [16]); (2) Contact and non-contact manipulation of non-magnetic microbead using the magnetic-based bilateral tele-manipulation system. The designed scaled tele-manipulation system is used in the positioning of non-magnetic microbeads with and without contact to achieve successful releases at the reference positions [17], [18]. This positioning is done by the operator and the interactions are sensed by scaling the forces up to the human tactile sensory range (approximately 0.8 mN [19]).

The remainder of this paper is organized as follows: Section II provides descriptions of the haptic device and the electromagnetic system. The design of the tele-manipulation control system is included in Section III. Experimental results are included in Section IV. Finally, Section V concludes and provides direction for future work.

II. ELECTROMAGNETIC-BASED BILATERAL TELE-MANIPULATION SYSTEM

The bilateral tele-manipulation system consists of a haptic device and an electromagnetic system with an orthogonal configuration of 4 electromagnetic coils (Fig. 1). The workspaces of these two systems are analyzed and connected using a tele-manipulation system.

A. Characterization of the Workspaces

Our haptic device is a pantograph mechanism, the length of each link is denoted by l_i, for $i = 0, \ldots, 4$. The angular position of each link is measured with respect to a fixed reference frame and is indicated using, q_i. The haptic device contains 2 active angles ($\mathbf{q}_\mathrm{a} = [q_1 \quad q_4]^\mathrm{T}$) and 2 passive angles ($\mathbf{q}_\mathrm{p} = [q_2 \quad q_3]^\mathrm{T}$). The holonomic constrains of the haptic device are given by

$$\begin{bmatrix} \underbrace{l_1 \cos q_1 + l_2 \cos q_2}_{x_\mathrm{e}} - l_3 \cos q_3 - l_4 \cos q_4 - l_0 \\ \underbrace{l_1 \sin q_1 + l_2 \sin q_2}_{y_\mathrm{e}} - l_3 \sin q_3 - l_4 \sin q_4 \end{bmatrix} = 0, \quad (1)$$

where $\mathbf{x} = [x_\mathrm{e} \quad y_\mathrm{e}]^\mathbf{T}$ is the position of the end-effector, and x_e and y_e are its coordinates. Taking the time-derivative of (1) in the frame of reference and representing $\dot{\mathbf{x}}$ using the active angles yields

$$\dot{\mathbf{x}} = \underbrace{\begin{bmatrix} -l_1 \sin q_1 - \frac{l_1 \sin q_2 \sin(q_3 - q_1)}{\sin(q_2 - q_3)} & \frac{l_4 \sin q_2 \sin(q_3 - q_4)}{\sin(q_2 - q_3)} \\ l_1 \cos q_1 + \frac{l_1 \cos q_2 \sin(q_3 - q_1)}{\sin(q_2 - q_3)} & \frac{l_4 \cos q_2 \sin(q_3 - q_4)}{\sin(q_2 - q_3)} \end{bmatrix}}_{\mathbf{J}(\mathbf{q})} \dot{\mathbf{q}}_\mathrm{a}, \quad (2)$$

where $\dot{\mathbf{x}} \in \mathbb{R}^{2\times 1}$ is the velocity of the end-effector in the frame of reference. Further, $\mathbf{J}(\mathbf{q}) \in \mathbb{R}^{2\times 2}$ is the Jacobian matrix of the haptic device that maps the angular velocities of the active angles only onto Cartesian velocities, and $\mathbf{q} \in \mathbb{R}^{4\times 1}$ is a vector of its generalized coordinates. We use (2) to map joint-space torques onto task-space forces as follows [20]:

$$\tau_\mathrm{m} = \mathbf{J}^\mathrm{T}(\mathbf{q}) \mathbf{F}_\mathrm{m}, \quad (3)$$

where $\tau_\mathbf{m} \in \mathbb{R}^{2\times 1}$ and $\mathbf{F}_\mathrm{m} \in \mathbb{R}^{2\times 1}$ are vectors of the input torques and task-space forces, respectively. The task-space forces are not homogenous within the entire workspace (black boundary in Fig. 2) of the haptic device, and it is desirable to limit this workspace to a region in which forces are almost homogenous. We calculate the task-space forces using (3) at 60 representative points within the workspace of the haptic device, as shown in Fig. 2. The gray square indicates a region where the task-space forces are almost uniform. This area is calculated to be 10 cm $\times$ 10 cm, and the motion of the operator is confined within this workspace.

On the other hand, the electromagnetic system contains a water reservoir in the middle of an orthogonal configuration of electromagnetic coils. This reservoir contains the slave-microrobot and non-magnetic microbeads at the water-air interface. The planar magnetic force ($\mathbf{F_s}(\mathbf{P}) \in \mathbb{R}^{2\times 1}$) exerted on the magnetic dipole moment ($\mathbf{m}(\mathbf{P}) \in \mathbb{R}^{2\times 1}$) of the slave-microrobot is given by [21]

$$\mathbf{F_s}(\mathbf{P}) = (\mathbf{m}(\mathbf{P}) \cdot \nabla)\mathbf{B}(\mathbf{P}), \quad (4)$$

where $\mathbf{B}(\mathbf{P}) \in \mathbb{R}^{2\times 1}$ is the planar magnetic field at the position of the slave-microrobot ($\mathbf{P} \in \mathbb{R}^{2\times 1}$). Kummer *et al.* have shown that the magnetic field can be mapped onto current input as follows [12]:

$$\mathbf{B}(\mathbf{P}) = \begin{bmatrix} B_x(\mathbf{P}) \\ B_y(\mathbf{P}) \end{bmatrix} = \begin{bmatrix} \tilde{\mathbf{B}}_x(\mathbf{P}) \\ \tilde{\mathbf{B}}_y(\mathbf{P}) \end{bmatrix} \begin{bmatrix} I_1 \\ \vdots \\ I_4 \end{bmatrix} = \widetilde{\mathbf{B}}(\mathbf{P})\mathbf{I}, \quad (5)$$

where $B_x(\mathbf{P}) \in \mathbb{R}^{1\times 1}$ and $B_y(\mathbf{P}) \in \mathbb{R}^{1\times 1}$ are the magnetic field components along x- and y-axis, respectively. $\tilde{\mathbf{B}}_x(\mathbf{P}) \in \mathbb{R}^{4\times 1}$ and $\tilde{\mathbf{B}}_y(\mathbf{P}) \in \mathbb{R}^{4\times 1}$ map the input current onto magnetic fields along x- and y-axis, respectively. Further, I_j, for $j = 1, \ldots, 4$, is the current input to the kth electromagnetic coil. $\widetilde{\mathbf{B}}(\mathbf{P}) \in \mathbb{R}^{2\times 4}$ is the magnetic field-current map and $\mathbf{I} \in \mathbb{R}^{4\times 1}$ is the input current vector. Substituting (5) in (4) yields

$$\begin{aligned} \mathbf{F_s}(\mathbf{P}) &= \left(m_x(\mathbf{P}) \frac{\partial}{\partial x} + m_y(\mathbf{P}) \frac{\partial}{\partial y} \right) \widetilde{\mathbf{B}}(\mathbf{P})\mathbf{I}, \quad (6) \\ &= \mathbf{\Lambda}(\mathbf{m}, \mathbf{P})\mathbf{I}, \quad (7) \end{aligned}$$

where $\mathbf{\Lambda}(\mathbf{m}, \mathbf{P}) \in \mathbb{R}^{2\times 4}$ is the actuation matrix which maps the input current onto magnetic force [12], [22]. We numerically calculate the magnetic field and field gradient within the workspace of the electromagnetic system using (6), and compare the calculated field to measurements using

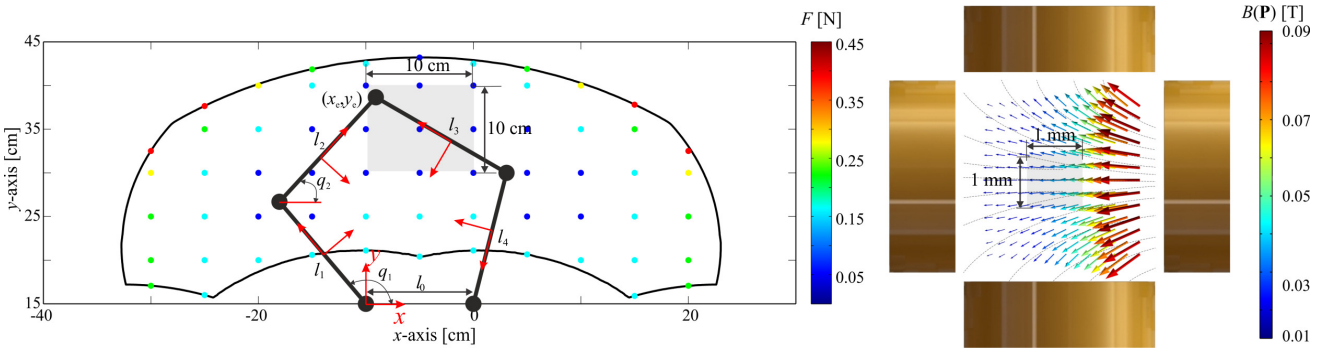

Fig. 2. The workspaces of the pantograph haptic interface (master-robot) and the electromagnetic system are 10 cm×10 cm and 1 mm×1 mm, respectively. The task-space forces of the end-effector of the haptic device are calculated using the Jacobian matrix and the maximum torques provided at the joint-space, using (2). The forces within the task-space of the haptic device are almost homogenous within the workspace (light gray rectangle). The magnetic field gradients of the electromagnetic system are calculated using a finite-element model. The magnetic forces are almost homogenous within the workspace (light gray square) of the electromagnetic system. The forces of the haptic device is calculated using Matlab (MathWorks, Natick, Massachusetts, U.S.A), whereas the magnetic fields are calculated using a calibrated finite element model using Comsol Multiphysics® (COMSOL, Inc., Burlington, U.S.A).

a calibrated 3-axis digital Teslameter (Senis AG, 3MH3A-0.1%-200mT, Neuhofstrasse, Switzerland). Agreement between the measured field and calculated field enables us to use (6) as a basis of the bilateral control system for the slave-side, whereas (3) is used to design the master-side of the bilateral control system. We also observe that the gradients are almost uniform within a workspace of 1 mm×1 mm. Therefore, we limit the motion of the slave-microrobot in this region during the bilateral tele-manipulation experiments.

B. Dynamics of the Haptic Device and Slave Microrobot

The haptic-device is a planar pantograph mechanism, the kinetic energies of its links (links 1 and 4) that exhibit rotational motion are given by

$$T_1 = \frac{1}{2}\frac{m_1 l_1^2}{3}\dot{q}_1^2 \quad \text{and} \quad T_4 = \frac{1}{2}\frac{m_4 l_4^2}{3}\dot{q}_4^2. \tag{8}$$

Link 2 undergoes translational and rotational motion. Therefore, its kinetic energy is given by

$$T_2 = \frac{m_2 l_2^2 \dot{q}_2^2}{24} + \frac{m_2}{2}\left(l_1^2\dot{q}_1^2 + \frac{l_2^2}{4}\dot{q}_2^2 + \frac{l_1 l_2}{2}\dot{q}_1\dot{q}_2 c_{12}\right), \tag{9}$$

where $c_{12} = \cos(q_1 - q_2)$. Similarly, the kinetic energy of link 3 is given by

$$T_3 = \frac{m_3 l_3^2 \dot{q}_3^2}{24} + \frac{m_3}{2}\left(l_4^2\dot{q}_4^2 + \frac{l_3^2}{4}\dot{q}_3^2 + \frac{l_3 l_4}{2}\dot{q}_3\dot{q}_4 c_{12}\right). \tag{10}$$

Using (8), (9), and (10), the total kinetic energy is, $T = \sum_{k=1}^{4} T_k$, and equation of motion of the haptic-device is calculated using

$$\frac{\mathrm{d}}{\mathrm{d}t}\left(\frac{\partial T}{\partial \dot{q}_k}\right) - \frac{\partial T}{\partial q_k} = Q_k \quad \text{for } k = 1, \ldots, 4, \tag{11}$$

where $Q_k = \mathbf{f}_\mathrm{o} \cdot \frac{\partial \mathbf{r}}{\partial q_k}$, is the kth generalized force associated with the kth generalized coordinate. $\mathbf{r}$ is a position vector of the end-effector, and $\mathbf{f}_\mathrm{o}$ is the input force from the operator. Based on (11), the dynamics of the master-robot in the joint-space is given by

$$\mathbf{H}_\mathrm{m}(\mathbf{q})\ddot{\mathbf{q}} + \mathbf{b}_\mathrm{m}(\mathbf{q}, \dot{\mathbf{q}})\dot{\mathbf{q}} = \tau_\mathrm{m} + \tau_\mathrm{o}, \tag{12}$$

where $\mathbf{H}_\mathrm{m}(\mathbf{q}) \in \mathbb{R}^{4\times4}$ and $\mathbf{b}_\mathrm{m}(\mathbf{q}, \dot{\mathbf{q}}) \in \mathbb{R}^{4\times4}$ are the inertia matrix and Coriolis damping of the master-robot, respectively. Further, $\tau_\mathrm{o} \in \mathbb{R}^{2\times1}$ is the interaction torque between the master-robot and the operator, respectively. In (12), $\mathbf{H}_\mathrm{m}(\mathbf{q})$ is given by

$$\mathbf{H}_\mathrm{m}(\mathbf{q}) = \begin{bmatrix} h_{11} & uc_{12} & 0 & 0 \\ uc_{12} & \frac{m_2 l_2^2}{3} & 0 & 0 \\ 0 & 0 & \frac{m_3 l_3^2}{3} & vc_{34} \\ 0 & 0 & vc_{34} & h_{44} \end{bmatrix}, \tag{13}$$

where $h_{11} = \left(\frac{m_1}{3} + m_2\right) l_1^2$, $h_{44} = \left(\frac{m_4}{3} + m_3\right) l_4^2$, $u = \frac{m_2 l_1 l_2}{4}$, $v = \frac{m_3 l_3 l_4}{4}$, and $c_{34} = \cos(q_3 - q_4)$. Further, $\mathbf{b}_\mathrm{m}(\mathbf{q}, \dot{\mathbf{q}})$ is given by

$$\mathbf{b}_\mathrm{m} = \begin{bmatrix} u\dot{q}_2 s_{12} & -uas_{12} & 0 & 0 \\ -uas_{12} & -u\dot{q}_1 s_{12} & 0 & 0 \\ 0 & 0 & v\dot{q}_4 s_{34} & -vbs_{34} \\ 0 & 0 & -vbs_{34} & v\dot{q}_3 s_{34} \end{bmatrix}, \tag{14}$$

where $a = \dot{q}_1 - \dot{q}_2$ and $b = \dot{q}_3 - \dot{q}_4$. Further, $s_{12} = \sin(q_1 - q_2)$ and $s_{34} = \sin(q_3 - q_4)$. Our objective is to scale the motion of the operator's hand to control a slave-microrobot remotely. Therefore, we project the equation of motion onto the task-space using (2) and (3), and obtain

$$\mathbf{M}_\mathrm{m}(\mathbf{q})\ddot{\mathbf{x}} + \mathbf{c}_\mathrm{m}(\mathbf{q}, \dot{\mathbf{q}})\dot{\mathbf{x}} = \mathbf{F}_\mathrm{m} + \mathbf{f}_\mathrm{o}, \tag{15}$$

where $\mathbf{M}_\mathrm{m}(\mathbf{q}) \in \mathbb{R}^{2\times2}$ is the inertia matrix of the haptic-device in the task-space and is given by

$$\mathbf{M}_\mathrm{m}(\mathbf{q}) = \mathbb{J}^{\mathrm{T}^{-1}}\mathbf{H}(\mathbf{q})\mathbb{J}^{-1} \text{ and } \mathbb{J} = \begin{bmatrix} \mathbf{J}(\mathbf{q}) & | & \mathbf{0}_{2\times2} \end{bmatrix}. \tag{16}$$

where $\mathbb{J} \in \mathbb{R}^{2\times4}$ is a Jacobian matrix that includes the passive links of the haptic device. In (15), $\mathbf{c}_\mathrm{m}(\mathbf{q}, \dot{\mathbf{q}})$ is given by

$$\mathbf{c}_\mathrm{m}(\mathbf{q}, \dot{\mathbf{q}}) = \mathbb{J}^\mathrm{T}\mathbf{b}_\mathrm{m}(\mathbf{q}, \dot{\mathbf{q}})\mathbb{J}^{-1} - \mathbb{J}^\mathrm{T}\mathbf{H}_\mathrm{m}(\mathbf{q})\mathbb{J}^{-1}\dot{\mathbb{J}}\mathbb{J}^{-1}. \tag{17}$$

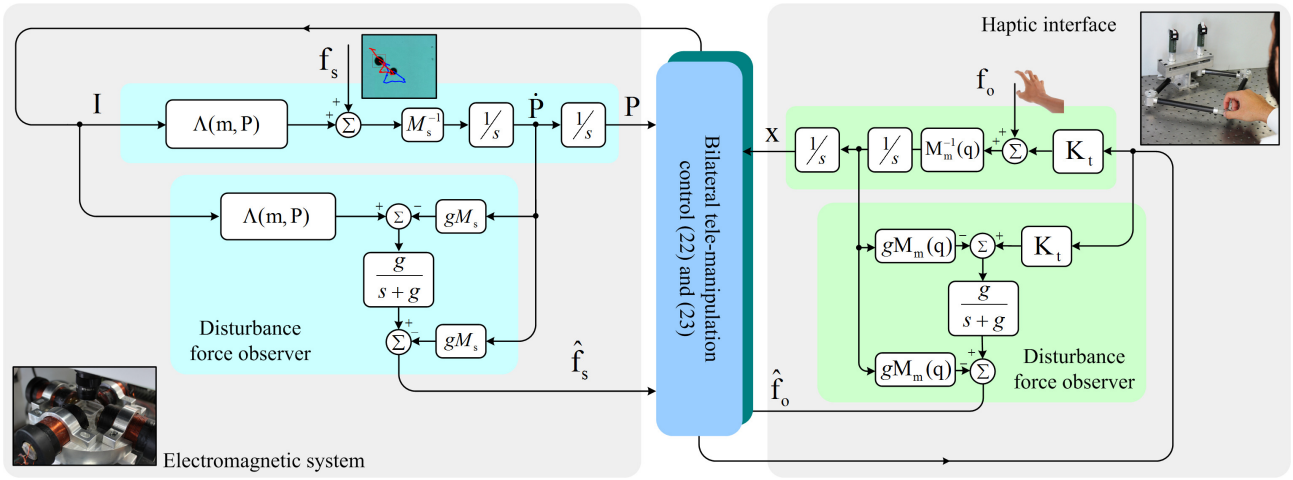

Fig. 3. The architecture of the scaled-bilateral tele-manipulation system between the master-robot (haptic device) and slave-microrobot (paramagnetic microparticles) [28]. The scaled bilateral tele-manipulation system is based on 4 inputs from the master-robot and slave-microrobot, i.e., position of the end-effector ($\mathbf{x}$), position of the microparticles ($\mathbf{P}$), the estimated interaction force between the end-effector and operator ($\hat{\mathbf{f}}_\mathrm{o}$), and the estimated interaction forces with the microparticles ($\hat{\mathbf{f}}_\mathrm{s}$). This control system scales down (by 2 orders on magnitude) the motion of the operator to control the microparticles (bottom-left corner) within a workspace of 1 mm $\times$ 1 mm. It also scales up (by 6 orders on magnitude) the estimated interaction forces of the microparticles to the sensory range of the operator (top-right corner).

Now we turn our attention to the slave-side, paramagnetic microparticles are used as slave-microrobots. These microparticles are influenced by several factors such as the external magnetic force, viscous drag force, inertia, Brownian motion, microparticle-fluid interaction, and magnetic dipole interactions between multiple microparticles. We assume that the magnetic force and the viscous drag force are dominant [23]. Therefore, the dynamics of the slave-microrobot is given by

$$M_\mathrm{s}\ddot{\mathbf{P}} + \mathbf{c}_\mathrm{s}(\dot{\mathbf{P}}) = \mathbf{F_s}(\mathbf{P}) + \mathbf{f}_\mathrm{s}. \tag{18}$$

In (5), M_s and $\mathbf{c}_\mathrm{s}(\dot{\mathbf{P}}) \in \mathbb{R}^{2\times1}$ are the mass of the slave-microrobot and the damping force on the slave-microrobot, respectively. Further, $\mathbf{f}_\mathrm{s} \in \mathbb{R}^{2\times1}$ is the interaction force between the slave-microrobot and the environment. The influence of the inertial term $(M_\mathrm{s}\ddot{\mathbf{P}}) \in \mathbb{R}^{2\times1}$ is based on the Reynolds number of the slave-microrobot. We calculate the Reynolds number as $Re = \frac{\rho|\dot{\mathbf{P}}|L}{\mu} = 0.01$, where ρ is the density of the fluid (998.2 kg.m^{-3}), $\dot{\mathbf{P}}$ is the velocity of the slave-microrobot at order of $\mathcal{O}(10^2)$ μm/s, and L is its length (100 μm), and μ is the dynamic viscosity of the fluid (10^{-3} Pa.s). It is also possible to use a cluster of microparticles as slave-microrobot during tele-manipulation. Therefore, the lower-limit on Reynolds number is of order $\mathcal{O}(10^{-2})$.

III. Bilateral Tele-Manipulation System Design

We define position tracking error ($\mathbf{e}_\mathrm{p} \in \mathbb{R}^{2\times1}$) and force tracking error ($\mathbf{e}_\mathrm{f} \in \mathbb{R}^{2\times1}$) between the master-robot and slave-microrobot as follows:

$$\mathbf{e}_\mathrm{p} = \mathbf{x} - \alpha\mathbf{P} \quad \text{and} \quad \mathbf{e}_\mathrm{f} = \mathbf{f}_\mathrm{o} + \beta\mathbf{f}_\mathrm{s}, \tag{19}$$

where $\alpha > 0$ and $\beta > 0$ are position and force scaling coefficients, respectively. Using (19), we define a generalized position tracking error ($\sigma \in \mathbb{R}^{2\times1}$) as follows [24]-[27]:

$$\sigma = c\mathbf{e}_\mathrm{p} + \dot{\mathbf{e}}_\mathrm{p}. \tag{20}$$

In (20), c is a positive control gain. In order to achieve asymptotic convergence, we select the desired accelerations as

$$\Gamma_\mathrm{p} = -k_\mathrm{p}\sigma \quad \text{and} \quad \Lambda_\mathrm{f} = -k_\mathrm{f}D_\mathrm{h}^{-1}\mathbf{e}_\mathrm{f}, \tag{21}$$

where $\Gamma_\mathrm{p} \in \mathbb{R}^{2\times1}$ and $\Lambda_\mathrm{f} \in \mathbb{R}^{2\times1}$ are the desired accelerations in the position and force control-loops, respectively. The controller gains (k_p) and (k_f) are positive-definite and D_h is the damping coefficient of the operator hand. Finally, the control input at the master-robot is given by

$$\mathbf{F_m} = \frac{\widehat{\mathbf{M}}_\mathrm{m}(\mathbf{q})}{\alpha+\beta}\left(\alpha\Lambda_\mathrm{f} + \beta\Gamma_\mathrm{p}\right) + \hat{\mathbf{c}}_\mathrm{m}(\mathbf{q},\dot{\mathbf{q}})\dot{\mathbf{x}} - \hat{\mathbf{f}}_\mathrm{o}, \tag{22}$$

where $\widehat{\mathbf{M}}_\mathrm{m}(\mathbf{q})$ and $\hat{\mathbf{c}}_\mathrm{m}(\mathbf{q},\dot{\mathbf{q}}) \in \mathbb{R}^{2\times1}$ are the nominal inertial matrix and nominal Coriolis damping forces calculated using (16) and (17), respectively. In (22), $\hat{\mathbf{f}}_\mathrm{o}$ is the estimated interaction force between the master-robot and the operator. The control input at the slave-microrobot is calculated by setting the magnetic force $\mathbf{F_s}(\mathbf{P})$ to

$$\mathbf{F_s}(\mathbf{P}) = \frac{M_\mathrm{s}}{\alpha+\beta}\left(\Lambda_\mathrm{f} - \Gamma_\mathrm{p}\right) + \hat{\mathbf{c}}_\mathrm{s}(\dot{\mathbf{P}}) - \hat{\mathbf{f}}_\mathrm{s}. \tag{23}$$

In (23), $\hat{\mathbf{c}}_\mathrm{s}(\dot{\mathbf{P}}) \in \mathbb{R}^{2\times1}$ is the nominal damping force on the slave-microrobot. Further, $\hat{\mathbf{f}}_\mathrm{s} \in \mathbb{R}^{2\times1}$ is the estimated interaction force between the slave-microrobot and the environment. The scaled-bilateral control architecture is shown in Fig. 3. The bilateral control laws depend on 4 inputs (19), i.e., positions of the master-robot and the slave-microrobot, and the interaction forces between the operator and the

master-robot and the slave-microrobot and its surrounding environment. Substituting (22) in (15), we obtain

$$\ddot{\mathbf{x}} = \frac{1}{\alpha+\beta}\left(-\alpha k_{\mathrm{f}} D_{\mathrm{h}}^{-1}\mathbf{e}_{\mathrm{f}} - \beta k_{\mathrm{p}}\sigma\right). \tag{24}$$

Similarly, substituting (23) in (18) yields

$$\ddot{\mathbf{P}} = \frac{1}{\alpha+\beta}\left(-\alpha k_{\mathrm{f}} D_{\mathrm{h}}^{-1}\mathbf{e}_{\mathrm{f}} + k_{\mathrm{p}}\sigma\right). \tag{25}$$

Finally, the position tracking error of the bilateral control system is calculated using (24) and (25), as follows:

$$\ddot{\mathbf{e}}_{\mathrm{p}} = \ddot{\mathbf{x}} - \alpha\ddot{\mathbf{P}} = -k_{\mathrm{p}} c\mathbf{e}_{\mathrm{p}} - k_{\mathrm{p}}\dot{\mathbf{e}}_{\mathrm{p}}. \tag{26}$$

Therefore, the error dynamics between the master-robot and slave-microrobot is governed by

$$\ddot{\mathbf{e}}_{\mathrm{p}} + k_{\mathrm{p}}\dot{\mathbf{e}}_{\mathrm{p}} + k_{\mathrm{p}} c\mathbf{e}_{\mathrm{p}} = 0. \tag{27}$$

The control gains k_{p} and c have to achieve stable roots of the characteristic polynomial of (27), which can be represented in the following form:

$$\begin{bmatrix}\dot{\mathbf{e}}_{\mathrm{p}}\\ \ddot{\mathbf{e}}_{\mathrm{p}}\end{bmatrix} = \underbrace{\begin{bmatrix} 0 & 0 & 1 & 0\\ 0 & 0 & 0 & 1\\ -k_{\mathrm{p}}c & 0 & -k_{\mathrm{p}} & 0\\ 0 & -k_{\mathrm{p}}c & 0 & -k_{\mathrm{p}}\end{bmatrix}}_{\mathbf{A}} \begin{bmatrix}\mathbf{e}_{\mathrm{p}}\\ \dot{\mathbf{e}}_{\mathrm{p}}\end{bmatrix}. \tag{28}$$

In particular, the matrix $\mathbf{A}$ in (28) is Hurwitz; that is, its eigenvalues have strictly negative real parts. To study the stability of the force tracking error ($\mathbf{e}_{\mathrm{f}}$), we substitute $\mathbf{f}_{\mathrm{o}}$ and $\mathbf{f}_{\mathrm{s}}$ using (15) and (18) in the force tracking error (19), we obtain

$$\mathbf{e}_{\mathrm{f}} = \mathbf{M}_{\mathrm{m}}\ddot{\mathbf{x}} + \beta M_{\mathrm{s}}\ddot{\mathbf{P}} + \frac{k_{\mathrm{f}} D_{\mathrm{h}}^{-1}}{\alpha+\beta}\mathbf{e}_{\mathrm{f}}\left(\alpha\mathbf{M}_{\mathrm{m}} + \beta M_{\mathrm{s}}\mathbf{I}_{\mathrm{id}}\right) - \widehat{\mathbf{f}}_{\mathrm{o}} + \beta\widehat{\mathbf{f}}_{\mathrm{s}}, \tag{29}$$

where $\mathbf{I}_{\mathrm{id}} \in \mathbb{R}^{2\times 2}$ is the identity matrix. Substituting (24) into (29) yields

$$0 = \frac{M_{\mathrm{s}}}{\alpha+\beta}\beta k_{\mathrm{f}} D_{\mathrm{h}}^{-1}\mathbf{e}_{\mathrm{f}} - \frac{\beta k_{\mathrm{p}}}{\alpha+\beta}\mathbf{M}_{\mathrm{m}}\sigma + \beta M_{\mathrm{s}}\ddot{\mathbf{P}}. \tag{30}$$

The last term in (30) can be ignored because of the low Reynolds number characteristic. Therefore, force tracking error is coupled with the position tracking error using

$$\mathbf{e}_{\mathrm{f}} = \frac{k_{\mathrm{p}} c}{M_s k_{\mathrm{f}} D_{\mathrm{h}}^{-1}}\mathbf{M}_{\mathrm{m}}\mathbf{e}_{\mathrm{p}} + \frac{k_{\mathrm{p}}}{M_s k_{\mathrm{f}} D_{\mathrm{h}}^{-1}}\mathbf{M}_{\mathrm{m}}\dot{\mathbf{e}}_{\mathrm{p}} \tag{31}$$

$$= \frac{k_{\mathrm{p}}}{M_s k_{\mathrm{f}} D_{\mathrm{h}}^{-1}}\mathbf{M}_{\mathrm{m}}\underbrace{\begin{bmatrix} c & c & 0 & 0\\ 0 & 0 & 1 & 1\end{bmatrix}}_{\mathbf{C}}\begin{bmatrix}\mathbf{e}_{\mathrm{p}}\\ \dot{\mathbf{e}}_{\mathrm{p}}\end{bmatrix}. \tag{32}$$

It follows from (28) and (32) that

$$\|\mathbf{e}_{\mathrm{f}}\| \le \frac{k_{\mathrm{p}}}{M_s k_{\mathrm{f}} D_{\mathrm{h}}^{-1}}\|\mathbf{M}_{\mathrm{m}}\|\|\mathbf{C}\|\|e^{\mathbf{A}t}\mathbf{e}_{\mathrm{p}}(0)\|, \tag{33}$$

where $\|.\|$ denotes the maximum singular value operator norm and $\mathbf{e}_{\mathrm{p}}(0)$ is the initial value of position tracking error. Since $\mathbf{A}$ is Hurwitz, there exist $\xi > 0$ and $\chi > 0$ such that $\|e^{\mathbf{A}t}\mathbf{e}_{\mathrm{p}}(0)\| \le \xi e^{-\chi t}\|\mathbf{e}_{\mathrm{p}}(0)\|$. Further from (1) and (16), the map $\mathbf{x} \mapsto \mathbf{M}_{\mathrm{m}}(\mathbf{x})$ is positive definite and piecewise continuous, which implies that $\|\mathbf{M}_{\mathrm{m}}\|$ is uniformly bounded since (27) ensures that $\mathbf{x}$ is uniformly bounded. This in turn implies that

$$\|\mathbf{e}_{\mathrm{f}}\| \to 0 \quad \text{as} \quad t \to \infty. \tag{34}$$

The implementation of the scaled-bilateral tele-manipulation control is based on the estimation or measurement of the interaction forces between the operator and the end-effector, and the slave-microrobot and its surrounding environment (particles-to-particles interactions, drag force, and interaction force with non-magnetic microbeads). We estimate the interaction forces in the force tracking error (19) using DOBs [26], [27], [28]. The estimated interaction force ($\hat{\mathbf{f}}_{\mathrm{s}}$) on the slave-microrobot is given by

$$\hat{\mathbf{f}}_{\mathrm{s}} = \frac{g}{s+g}\left(\mathbf{F}_{\mathrm{s}}(\mathbf{P}) + gM_{\mathrm{s}}\dot{\mathbf{P}}\right) - gM_{\mathrm{s}}\dot{\mathbf{P}}, \tag{35}$$

where g is the gain of the low-pass filter, and $\mathbf{F}_{\mathrm{s}}(\mathbf{P})$ is the nominal magnetic force exerted on the slave-microrobot (6). The interaction force ($\hat{\mathbf{f}}_{\mathrm{o}}$) between the end-effector of the haptic device and the operator is estimated using the following DOB:

$$\hat{\mathbf{f}}_{\mathrm{o}} = \frac{g}{s+g}\left(\mathbf{K}_{\mathrm{t}}\mathbf{I}_{\mathrm{m}} + g\widehat{\mathbf{M}}_{\mathrm{m}}(\mathbf{q})\dot{\mathbf{x}}\right) - g\widehat{\mathbf{M}}_{\mathrm{m}}(\mathbf{q})\dot{\mathbf{x}}, \tag{36}$$

where $\mathbf{K}_{\mathrm{t}}$ is a matrix of the torque constants of the actuators. Further, $\mathbf{I}_{\mathrm{m}}$ is the input current vector to the haptic device. Fig. 3 provides the architecture of the DOBs (35) and (36). The output of the DOB of the slave-microrobot is validated by measuring the interaction forces between the slave-microrobot and the tip of a microforce sensing probe that is embedded within the electromagnetic system [29]. A compression force of 0.7 μN is measured when the slave-microrobot (3 paramagnetic microparticles) contacts the tip, whereas a non-contact force with an average of 0.3 μN is measured before the contact with the tip of the microforce sensing probe. This measurement is compared to the estimated force using (34) and we find agreement between the measured and estimated forces [14].

IV. EXPERIMENTAL RESULTS

Our tele-manipulation exprimental results are done using a pantograph haptic device and an electromagnetic system. The haptic device consists of 4 carbon fiber (35048-OW, Rock West Composites, Utah, U.S.A) tubes ($l_1 = l_4 =$ 150 mm and $l_2 = l_3 =$ 225 mm). The tubes are connected together to form a closed-configuration with a distance of 100 mm between the active tubes (diameter of 28.8 mm). The active tubes are actuated using two DC motors (2322 980, Maxon Motor, Sachseln, Switzerland). These motors have torque constant (k_{t}) of 15.3 mN.m.A^{-1} and rotor inertia of

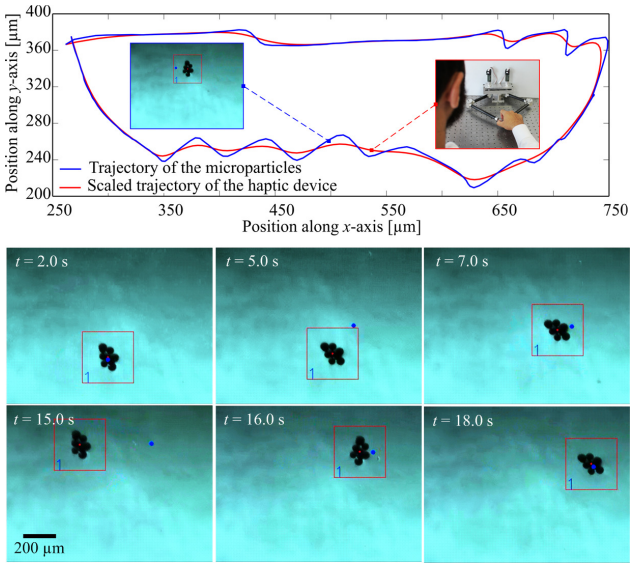

Fig. 4. A representative scaled-bilateral tele-manipulation experimental control result using a haptic device (master-robot) and a cluster of para-magnetic microparticles (slave-microrobot). The red square indicates the position of the slave-microrobot and is assigned using our feature tracking algorithm, whereas the small blue circle indicates the scaled position of the end-effector of the haptic device. *Please refer to the accompanying video.*

5.88 g.cm^2, and are controlled via an NI myRIO board (National Instruments, Austin, Texas, U.S.A). The position and forces of the end-effector are determined using the Jacobian matrix of the haptic device using (2) and (3), respectively. The electromagnetic system consists of 4 electromagnetic coils. Each coil is independently supplied with current input using electric driver (MD10C, Cytron Technologies Sdn. Bhd, Kuala Lumpur, Malaysia) and controlled via an Arduino control board (Arduino UNO - R3, Arduino, Memphis, Tennessee, U.S.A). The electromagnetic configuration contains a force sensor (FT S100 140305 29, FemtoTools AG, Buchs, Switzerland) to measure the interaction forces with the slave-microrobot. The force sensor is fixed using a three-dimensional motion stage (LDV40-LM-C2, SELN Dongguan Shengang Precision Metal & Electronic Co., Ltd.,Guangdong, China). Position of the slave-microrobot is determined using a stereo microscopic system (Stemi 2000-C, Carl Zeiss Microscopy, LLC, New York, U.S.A) and a Sony XCD-X710 (Sony Corporation, Tokyo, Japan) FireWire camera. The bilateral tele-manipulation system is mounted on a tuned damped optical table (M-ST-UT2-58-12, Newport, California, U.S.A).

The scaled trajectory of the operator and the current position of the slave-microrobot are used to calculate the position tracking error ($\mathbf{e}_\mathrm{p}$), whereas the estimated forces are used to calculate the force tracking error ($\mathbf{e}_\mathrm{f}$). Fig. 4 demonstrates the stability of the position tracking based on (27). The slave-microrobot (cluster of 6 microparticles) follows the scaled-position of the operator at an average speed of 100 μm/s. The red and blue lines represent the scaled trajectory of the operator and the trajectory of the slave-microrobot. In this representative trial, the position scaling coefficient (α) is set to 2285 and the force scaling coefficient (β) is set to 10^6. Table I provides the parameters and the control gains of the tele-manipulation system.

TABLE I

PARAMETERS AND CONTROL GAINS OF THE CONTROL SYSTEM.

Parameter	Value	Parameter	Value
α	2285	β	10^6
g [rad.s^{-1}]	10	k_t [mN.m.A^{-1}]	15.3
k_p [s^{-1}]	> 0	k_f [s^{-1}]	> 0
r_p [μm]	50	M_s [kg]	7.33×10^{-10}

We also use our magnetic-based tele-manipulation system to position non-magnetic microbeads (blue polystyrene particles, Micromod Partikeltechnologie GmbH, Rostock-Warnemuende, Germany). Fig. 5 provides a representative tele-manipulation experiment of the non-magnetic microbead towards a reference position (small orange circle). The positions of the slave-microrobot and the microbead are indicated using the red and blue lines, respectively (Fig. 5(a)). Positioning of the microbead is achieved via contact and non-contact manipulation between the microbead and the slave-microrobot. At time, $t = 7$ seconds, the slave-microrobot touches the microbead and changes its orientation towards the reference position. At time, t= 16 seconds, the slave-microrobot reverses its direction at a relatively high speed to break free from the adhesive force with the microbead [18]. This action enables non-contact pushing of the microbead by moving the slave-microrobot slowly with respect the microbead towards the reference position (time instants, t=17 seconds and t=18 seconds). Once the microbead is positioned at the reference position (t=20 seconds), the operator moves the slave-microrobot at relatively high speed away from the microbead to break free from the adhesive forces and to achieve a successful release. During this tele-manipulation experiment, the interaction forces are estimated, scaled-up, and sensed by the operator. The scaled-force on the master-robot and the interaction force on the slave-microrobot are shown in Fig. 5(b). In this trial, the non-contact pushing and pulling are used to accurately position the microbead within the vicinity of the reference position, and the maximum position tracking error is calculated to be 8 μm in the steady-state. Another tele-manipulation trial is provided in Fig. 6 without contact between the slave-microrobot and the non-magnetic microbead. Before time, t=12 seconds, the slave-microrobot achieves non-contact pushing to move the microbead, as shown in Fig. 6(a). At time, t=12 seconds, the direction of slave-microrobot is reversed to achieve non-contact pulling to position the microbead at the reference position (Fig. 6(b)). These non-contact pushing and pulling forces are also scaled-up to the sensory range of the operator and are detected during the manipulation trial, as shown in Fig. 6(c). *Please refer to the accompanying video.*

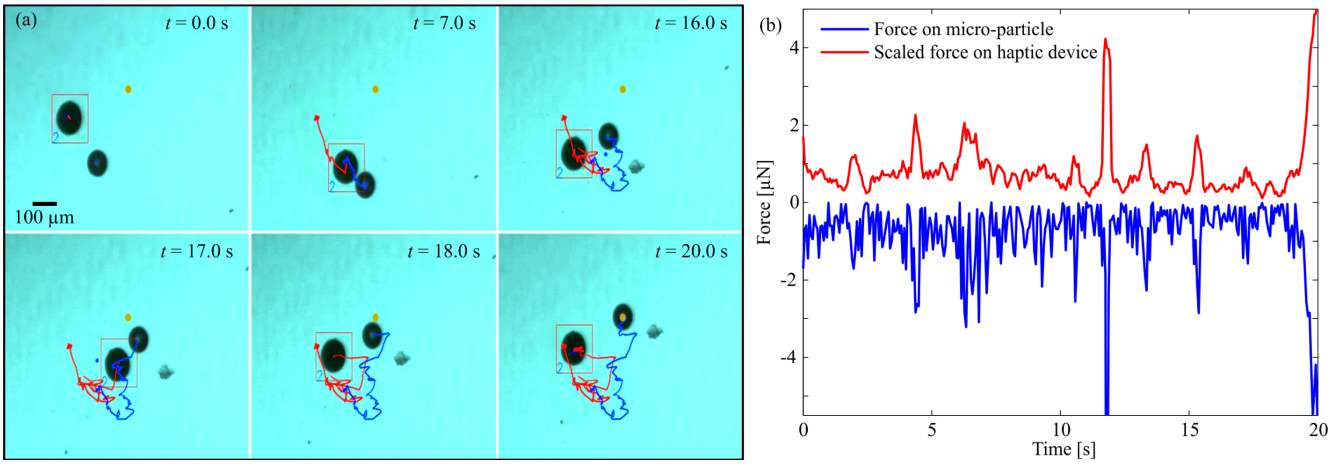

Fig. 5. A representative bilateral tele-manipulation of a non-magnetic microbead with average diameter of 100 μm using a slave-microrobot. (a) Tele-manipulation of the microbead is achieved via contact and non-contact pushing and pulling. The red and blue lines indicate the paths of the slave-microrobot and the microbead, respectively. (b) The operator senses the interaction forces between the slave-microrobot and the microbead after scaling this force up to his sensory range. The interaction forces are estimated using (35) and (36). The bilateral tele-manipulation enables localization of the microbead within the vicinity of a reference position (small orange circle). *Please refer to the accompanying video.*

The utilization of DOBs in the implementation of tele-manipulation control system enables the operator to sense the interaction forces while still being in control (Figs. 5 and 6). The estimated force at the slave-microrobot provides the operator with qualitative information from the environment of the slave-side. We assume that the viscous drag and microbead-to-microparticle interaction forces are dominant based on the calculated Reynolds number. Although Figs. 5(b) and 6(c) show good agreement between the estimated forces using the DOBs (based on the stability of the force tracking error (34)), we do not yet have a clear understanding of the nature of the sensed forces at the haptic interface. In the representative trial shown in Fig. 5, a non-contact force of 0.75 μN is estimated when the distance between the slave-microrobot and microbead is controlled (by the operator) to be approximately 100 μm. At time, t=7 seconds, contact between the slave-microrobot and the microbead is observed and we also find a microbead force of 2 μN that is sensed by the operator (after scaling). At time, t=12 seconds and t= 20 seconds we observe two peaks of 4.0 μN and 4.5 μN, respectively. These peaks are due to the increased viscous drag force due to the increased speed of the slave-microrobot. The operator increases the speed of the slave-microrobot to break free from the contact with the microbead. Therefore, greater drag force is estimated and sensed by the operator. At time, t=20 seconds, the operator increases the speed of the slave microrobot to achieve a successful release of the microbead at the reference position (small orange circle). Therefore, the drag force is also increased and observed as a peak of 4.5 μN in the force estimated by the DOB.

V. CONCLUSIONS AND FUTURE WORK

This study presents a bilateral tele-manipulation system that enables accurate positioning of non-magnetic microbeads with and without contact. The operator stays in control of the manipulation while his accuracy is improved and the interaction forces are estimated via DOBs and scaled-up to his sensory range. This tele-manipulation system is designed based on a haptic device and an electromagnetic system with orthogonal configuration. We demonstrate bilateral contact and non-contact pushing and pulling to position microbeads with maximum position error of 8 μm. In addition, successful releases of the microbeads are achieved at the reference positions.

As part of future studies, the influence of the interaction force on the tele-manipulation experiments will be investigated and we will design a robust motion control system to account for the deviations between the nominal parameters used in the control inputs and the real model. Our system will be modified to enable tele-manipulation in three-dimensional space [30]. This modification is essential to achieve complex microassembly tasks. In addition, the transparency of the tele-manipulation and the effect of time-delay on the stability of the control system will be studied.

REFERENCES

[1] J.-B. Mathieu and S. Martel, "Steering of aggregatring magnetic microparticles using propulsion gradient coils in an MRI scanner," *Magnetic Resonance Medicine*, vol. 63, no. 5, pp. 1336-1345, May 2010.

[2] I. S. M. Khalil, F. van den Brink, O. S. Sukas, and S. Misra, "Microassembly using a cluster of paramagnetic microparticles," in *Proceedings of the IEEE International Conference on Robotics and Automation (ICRA)*, pp. 5507–5512, Karlsruhe, Germany, May 2013.

[3] J. J. Abbott, Z. Nagy, F. Beyeler, and B. J. Nelson, "Robotics in the small, part I: microbotics," *IEEE Robotics and Automation Magazine*, vol. 14, no. 2, pp. 92–103, June 2007.

[4] W. H. Wang, X. Y. Liu, and Y. Sun, "Autonomous zebrafish embryo injection using a microrobotic system," *IEEE Conference on Automation Science and Engineering*, pp. 363–368, Scottsdale, USA, September 2007.

[5] Y. Xie, D. Sun, C. Liu, H. Y. Tse, and S. H. Cheng, "A force control approach to a robot-assisted cell microinjection system," in

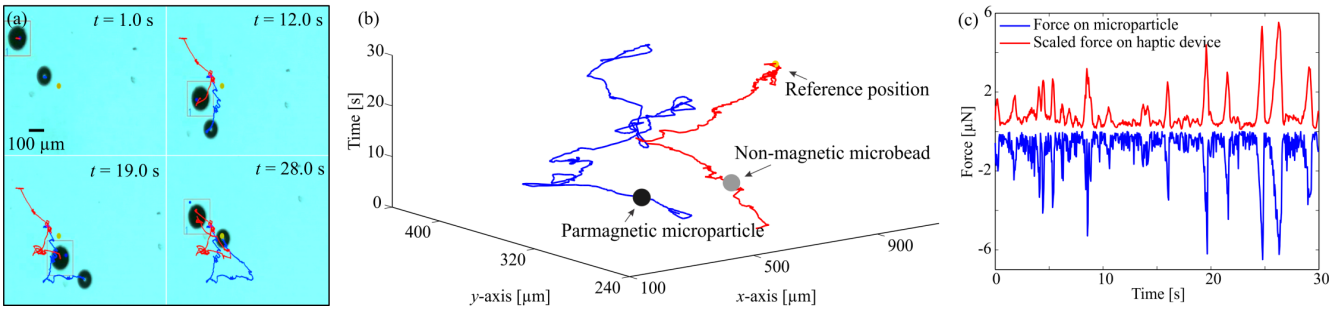

Fig. 6. A representative bilateral tele-manipulation of a non-magnetic microbead with average diameter of 100 μm using a slave-microrobot. (a) Tele-manupulation is achieved and the microbead is positioned within the vicinity of the reference position (small orange circle) via non-contact pushing and pulling. (b) The bilateral tele-manipulation enables localization of the microbead within the vicinity of a reference position. The non-contact forces enables successful release of the microbead at the reference position. The red and blue lines indicate the paths of the slave-microrobot and the microbead, respectively. (c) The operator senses the interaction forces between the slave-microrobot and the microbead after scaling this force up to his sensory range. The interaction forces are estimated using (35) and (36). *Please refer to the accompanying video.*

The International Journal of Robotics Research, vol. 29, no. 9, 2010, pp. 322–331, November 2009.

[6] B. J. Nelson, I. K. Kaliakatsos, and J. J. Abbott, "Microrobots for minimally invasive medicine," *The Annual Review of Biomedical Engineering*, vol. 12, pp. 55–85, April 2010.

[7] R. G. McNeil, R. C. Ritter, B. Wang, M. A. Lawson, G. T. Gillies, K. G. Wika, E. G. Quate, M. A. Howard, and M. S. Grady, "Characteristics of an improved magnetic-implant guidance system," *IEEE Transactions on Biomedical Engineering*, vol. 42, no. 8, pp. 802–808, August 1995.

[8] T. Lu, C. Pacoret, D. Hériban, A. Mohand-Ousaid, S. Régnier, and V. Hayward, "KiloHertz bandwidth, dual-stage haptic device lets you touch brownian motion," *IEEE Transactions On Haptics*, no. 99, pp. 1939–1412, December 2016.

[9] A. Pillarisetti, W. Anjum, J. P. Desai, G. Friedman, and A. D. Brooks, "Force feedback interface for vell injection," in *Procceding of the Joint Eurohaptics Symposium on Haptic Interfaces for Virtual Environment and Teleoperator Systems*, pp. 391–400, Pisa, Italy, March 2005.

[10] A. Pillarisetti, M. Pekarev, A. D. Brooks, and J. P. Desai, "Evaluating the effect of force feedback in cell injection", *IEEE/ASME Transactions on Automation Science and Engineering*, vol. 4, no. 3, pp. 322–331, July 2007.

[11] Y. Sun and B. J. Nelson, "Biological cell injection using an autonomous microrobotic system," in *The International Journal of Robotics Research*, vol. 21, no. 10-11, pp. 861–868, October 2002.

[12] M. P. Kummer, J. J. Abbott, B. E. Kartochvil, R. Borer, A. Sengul, and B. J. Nelson, "OctoMag: an electromagnetic system for 5-DOF wireless micromanipulation," *IEEE Transactions on Robotics*, vol. 26, no. 6, pp. 1006–1017, December 2010.

[13] A. Bolopion, H. Xie, D. S. Haliyo, and S. Régnier, "Haptic teleoperation for 3-D microassembly of spherical objects," in *IEEE/ASME Transactions on Mechatronics*, vol. 17, no. 1, pp. 116–127, December 2010.

[14] I. S. M. Khalil, Y. Michel, B. Su, and S. Misra, "Feeling paramagnetic micro-particles trapped inside gas bubbles: a tele-manipulation study," in *IEEE International Conference on Manipulation, Manufacturing and Measurement on the Nanoscale (3M-NANO)*, pp. 225-230, Chongqing, China, July 2016.

[15] I. S. M. Khalil, R. M. P. Metz, L. Abelmann, and S. Misra, "Interaction force estimation during manipulation of microparticles," in *Proceedings of the IEEE/RSJ International Conference of Robotics and Systems (IROS)*, pp. 950–956, Vilamoura, Algarve, Portugal, October 2012.

[16] I. S. M. Khalil and A. Sabanovic, "Sensorless action-reaction-based residual vibration suppression for multi-degree-of-freedom flexible systems," *Annual Conference of the IEEE Industrial Electronics Society (IECON)*, pp. 1633–1638, November 2010.

[17] S. Floyd, C. Pawashe, and M. Sitti, "Two-dimensional contact and noncontact micromanipulation in liquid using an untethered mobile magnetic microrobot," *IEEE Transactions on Robotics*, vol. 25, no. 6, pp. 1332–1342, December 2009.

[18] A. G. El-Gazzar, L. E. Al-Khouly, A. Klingner, S. Misra, and I. S. M. Khalil, "Non-Contact manipulation of microbeads via pushing and pulling using magnetically controlled clusters of paramagnetic microparticles," in *Proceedings of the IEEE/RSJ International Conference of Robotics and Systems (IROS)*, pp. 778–783, Hamburg, Germany, September 2015.

[19] G. C. Burdea, "Haptic feedback for virtual reality", *Virtual Reality and Prototyping Workshop*, Laval, France, June 1999.

[20] O. Khatib, "A unified approach for motion and force control of robot manipulators: The operational space formulation," *IEEE Journal on Robotics and Automation*, vol. 3, no. 1, pp. 43–53, March 1987.

[21] S. S. Shevkoplyas, A. C. Siegel, R. M. Westervelt, M. G. Prentiss, and G. M. Whitesides, "The force acting on a superparamagnetic bead due to an applied magnetic field," *Lab on a Chip*, vol. 7, no. 10, pp. 1294-1302, July 2007.

[22] J. J. Abbott, O. Ergeneman, M. P. Kummer, A. M. Hirt, and B. J. Nelson, "Modeling magnetic torque and force for controlled manipulation of soft-magnetic bodies," *IEEE Transactions on Robotics and Automation*, vol. 23, no. 6, pp. 1247-1252, December 2007.

[23] E. P. Furlani and K. C. Ng, "Analytical model of magnetic nanoparticle transport and capture in the microvasculature," *Physical Review*, vol. 73, no. 6 (061919), June 2006.

[24] Y. Yokokohji and T. Yoshikawa, "Bilateral control of master-slave manipulators for ideal kinesthetic coupling-formulation and experiment," *IEEE Transactions on Robotics and Automation*, vol. 10, no. 5, 1994, pp. 605–620, October 1994.

[25] D. A. Lawrence, "Stability and transparency in bilateral teleoperation," *IEEE Transactions on Robotics and Automation*, vol. 9, no. 5, pp. 624–637, October 1993.

[26] I. S. M. Khalil, H. Abass, M. Shoukry, A. Klingner, R. M. El-Nashar, M. Serry, and S. Misra, "Robust and optimal control of magnetic microparticles inside fluidic channels with time-varying flow rates", *International Journal of Advanced Robotic Systems*, vol. 13, no. 123, June 2016.

[27] T. Murakami and K. Ohnishi, "Observer-based motion control application to robust control and parameter identication," *Asia-Pacific Workshop on Advances in Motion Control (AMC)*, pp. 1–6, July 1993.

[28] I. S. M. Khalil, L. Abelmann, and S. Misra, "Magnetic-based motion control of paramagnetic microparticles with disturbance compensation," *IEEE Transactions on Magnetics*, vol. 50, no. 10 (5400110), October 2014.

[29] M. Elfar, M. Ayoub, A. Sameh, H. Abass, R. M. Abdel-Kader, I. Gomaa, and I. S. M. Khalil, "Targeted penetration of MCF-7 cells using iron-oxide nanoparticles *in vitro*", in *Proceedings of the IEEE RAS/EMBS International Conference on Biomedical Robotics and Biomechatronics (BioRob)*, pp. 260-265, Singapore, June 2016.

[30] I. S. M. Khalil, R. M. P. Metz, B. A. Reefman, and S. Misra, "Magnetic-Based minimum input motion control of paramagnetic microparticles in three-dimensional space," in *Proceedings of the IEEE/RSJ International Conference of Robotics and Systems (IROS)*, pp. 2053-2058, Tokyo, Japan, November 2013.